JTTEE5 15:72-82
DOI: 10.1361/105996306X92631
1059-9630/$19.00 © ASM International

Peer Reviewed

High-Power Hybrid Plasma Spraying of Large Yttria-Stabilized Zirconia Powder

Heji Huang, Keisuke Eguchi, and Toyonobu Yoshida

(Submitted March 2, 2005; in revised form September 2, 2005)

To testify to the advantage of large ceramic powder spraying, numerical simulations and experimental studies on the behavior of large yttria-stabilized zirconia (YSZ) powder in a high-power hybrid plasma spraying process have been carried out. Numeric predictions and experimental results showed that, with the high radio frequency (RF) input power of 100 kW, the most refractory YSZ powder with particle sizes as large as 88 µm could be fully melted and well-flattened splats could be formed. A large degree of flattening (ξ) of 4.7 has been achieved. The improved adhesive strength between the large splat and the substrate was confirmed based on the measurement of the crack density inside of the splats. A thick YSZ coating >300 µm was successfully deposited on a large CoNiCrAlY-coated Inconel substrate (50 × 50 × 4 mm in size). The ultra-dense microstructure without clear boundaries between the splats and the clean and crack-free interface between the top-coat and the bond-coat also indicate the good adhesion. These results showed that high-power hybrid plasma spraying of large ceramic powder is a very promising process for deposition of high-quality coatings, especially in the application of thermal barrier coatings (TBCs).

Keywords crack density, flattening degree, hybrid plasma, large powder spraying, single-splat deformation, thermal barrier coatings, thermal plasma spray

1. Introduction

Versatility and cost-efficiency have made thermal spraying an attractive coating technique that allows many problems of wear, corrosion, and thermal degradation to be resolved by engineering the component surface with tailor-made coatings (Ref 1). Above all, state-of-the-art atmospheric plasma sprayed (APS) thermal barrier coatings (TBCs) have been widely applied to improve the working efficiency of gas turbines and diesel engines or to prolong their lifetimes (Ref 2, 3). However, there is still much to be done to attain better coating quality to meet the requirements of long-term stability under more severe environments. For example, conventional TBCs deposited by APS are highly defective, containing various kinds of pores and cracks. These defects clearly contribute to the decrease of the thermal conductivity and also cause crack initiation, decrease the coating toughness, and eventually promote failure. To make matters worse, such defects originate naturally in the conventional APS process and make it difficult to control the structure by changing the limited parameters relating the process (Ref 4, 5). The most successive approach to improve the strain tolerance of the APS TBCs is considered to be the so-called "dense vertically cracked (DVC) TBC" invented by Taylor (Ref 6). The DVC TBC has a density at least 88% of the theoretical, wherein a plurality of vertical cracks are produced. The denser microstructure with the dominant vertical crack network system appears to benefit the erosion resistance and the strain tolerance

Nomenclature

C	constant
d	initial droplet diameter
D_0	initial particle diameter
D_h	diameter of the substrate holder
D_p	diameter of the plasma flame
F_p	powder feeding rate
n	substrate rotation speed
R	radial position
R_a	arithmetical mean roughness
Re	Reynolds number
R_s	thermal resistance between the droplet and the substrate
t	constant
T_d	droplet temperature
T_{es}	estimated substrate temperature
u	axial velocity of the droplet
V_d	droplet velocity
Z	axial position

Greek Symbols

θ	contact angle between the droplet and the substrate
ξ	flattening degree of a droplet
Λ	percentage of the substrate covered in one turn of rotation
η	viscosity
ψ	sphericity of the particle

Abbreviations

APS	atmospheric plasma spray
DC plasma	direct current plasma
DVC	dense vertically cracked
FE-SEM	field emission scanning electron microscope
FIB-SEM	focused ion beam scanning electron microscope
HVOF	high-velocity oxy fuel
RF plasma	radiofrequency plasma
TBCs	thermal barrier coatings
VOF	volume of fluid
YSZ	yttria-stabilized zirconia

Heji Huang, Keisuke Eguchi, and **Toyonobu Yoshida,** Department of Materials Engineering, the University of Tokyo, Hongo, 7-3-1, Bunkyo-ku, Tokyo, Japan, 113-8656. Contact e-mail: huang@plasma.t.u.-tokyo.ac.jp.

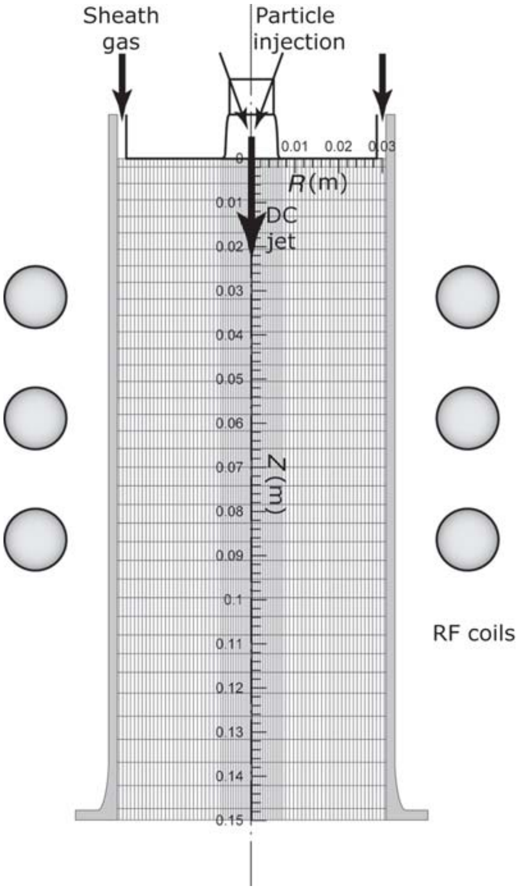

Fig. 1 Torch geometry and mesh used for the hybrid plasma calculations

and thus offers optimization of processing economics, appropriateness, and performance (Ref 7-9). To further increase thermal fatigue resistance, however, it is essential to increase the adhesive strength at the splat/substrate as well as the splat/splat interfaces by minimizing the extent of the horizontal cracks. In this respect, large-size powder spraying is worthy of investigation; as suggested by Yoshida et al. (Ref 10, 11), spraying of large-size powders might make it possible to deposit more dense and more adhesive coatings compared with the conventional spraying of small powders due to the higher substrate temperature under larger splat, which may also promote diffusive adhesion. Actually, the adhesive strength between a Ti splat and a stainless substrate was reported to be improved from 40 to 200 MPa when the particle size of the feedstock Ti powder was increased from 30 to 120 μm (Ref 11). Unfortunately, only a few papers have reported such larger powder size effects on the coating structures and properties in the case of ceramics. The main reason is considered to be the fact that the larger ceramics powders, especially YSZ, cannot be fully melted by conventional plasma spraying systems. Specifically, the current level of the plasma spraying equipment is not yet sufficient to respond to such demands.

Regarding the plasma spraying techniques, the most important issue lies on how to control the various distributions in the process. For a direct current (DC) plasma system, an intrinsic variation of the plasma intensity always exists due to the arc discharge characteristics, and the fluctuation period is almost the same as the time required for injected particles to be heated and melted (Ref 12), which makes it almost impossible to achieve homogeneous particle heating in a DC plasma. In addition, existence of electrodes also prevents the axial feeding of powder and leads to drastically distributed powder trajectories. For a

Table 1 Initial conditions and physical properties used in this research

	Simulations			Experiments	
	Hybrid plasma	**Particle thermal history**	**Droplet deformation**	**Single splat**	**Thick coating**
Initial powder (droplet) size d, μm	…	63, 71, 79, 88 Sphericity: 1, 0.8, 0.9	30, 63, 88	63-88	63-88
Initial powder (droplet) injection velocity, m/s	…	Axial velocity U_p: 10 Radial velocity V_p: +1.25, +2.5, +3.75	10, 30, 50, 70	…	…
Droplet temperature T_d, K	…	…	3000, 4573	…	…
Powder feeding rate F_p, g/min	…	10	…	4	10
Carrier gas flow rate F_c, slm	…	…	…	4	4
DC plasma power, kW	7 Efficiency: 40%	…	…	7	7
RF plasma power, kW	100, 60 Efficiency: 60%	…	…	100	100
DC plasma gas flow rate F_d, slm	Ar: 10	…	…	Ar: 10	Ar: 10
Sheath gas flow rate F_s, slm	Ar: 170 H_2: 30	…	…	Ar: 170 H_2: 30	Ar: 170 H_2: 30
Chamber pressure P, Pa	4×10^{-4}	…	…	4×10^{-4}	4×10^{-4}
Deposition distance L, mm	…	…	…	120	120
Substrate material	…	…	Stainless steel	Stainless steel	CoNiCrAlY-coated Inconel
Substrate rotation speed n, rpm	…	…	…	50	50
Estimated substrate surface temperature T_{es}, K	…	… …	800	723, 823, 923, 1123	823-923
Deposition time	…	…	…	10 s	10 min
Thermal contact resistance between droplet and substrate R, W/m^2·K	…	…	1×10^{-5}	…	…
Contact angle between droplet and substrate θ, degrees	…	…	45	…	…
Surface tension of zirconia, J/m^2	…	…	0.43	…	…

radiofrequency (RF) plasma system, the most notable feature is that the plasma volume is fairly large with diameter on the order of tens of millimeters, and the powder can be fed in the axial direction to narrow the distribution of particle trajectory and thermal history. The spraying yield of the RF system is as high as 80%. However, the velocity of the RF plasma is somewhat too low and resolidification of the droplets occurs occasionally. In recent years, development of other spraying techniques, such as the high-velocity oxy fuel (HVOF) system, the D-gun, and the hybrid plasma system, has enabled further control of the distributions in plasma spraying process. For example, compared with the conventional DC and RF plasma, the hybrid plasma is considered to be more feasible for thermal plasma spraying due to its large plasma volume, proper plasma velocity, high uniformity, and stability (Ref 13). In this research, therefore, we have developed a 150-kW hybrid plasma spraying system and tried to characterize large YSZ powder plasma spraying on the basis of numerical simulations and experimental studies.

2. Theoretical

2.1 General

A comprehensive thermal plasma spraying process, including hybrid plasma generation, powder heating, and splat formation, was simulated in this research. For the first two processes, a commercial code from Simulent Inc. (Ref 14) was used. In the case of splat formation, the code described in Ref 10 was used. The flow field of the plasma jet was first calculated based on a time-dependent governing model. The particle thermal history in such a plasma flame was then calculated. Because the presence of particles in the thermal plasma affects the plasma flow field by changing the thermodynamic and transport properties or by changing the mass, momentum and energy transport, coupling between the free plasma jet calculations and the particle thermal history calculations were repeated until convergence was attained. The ranges of the temperatures and velocities of the calculated droplets were then used as the initial conditions in the simulation of droplet deformation and solidification by solving the full Navier-Stokes and energy equations coupled with the volume of fluid (VOF) approach (Ref 10).

2.2 Torch Geometry and Simulation Details

Both simulations and experiments were conducted based on a novel 150-kW hybrid plasma spraying system. System specifications and details of the hybrid plasma torch have been described elsewhere (Ref 15). Figure 1 shows the torch geometry and the grid used in this analysis. The mesh size was chosen to be small enough to represent the gradients of pressure, velocity, and temperature that exist in the flow field.

The operating conditions and assumptions for the numerical simulations are summarized in Table 1. The efficiencies of the DC and the RF power units were assumed to be 40 and 60%, respectively. Zirconia powders with four initial sizes (D_0) of 63, 71, 79, and 88 μm and three different sphericities (ψ) of 0.8, 0.9, and 1.0 were injected into the hybrid plasma from the center of the torch at the position of (0.001, 0.001). ψ is defined as the ratio of the surface areas of a spherical particle and an actual particle with the same volume and was taken into the simulation as an amendment for the calculations of the heat transfer coefficient and the viscous drag coefficient (Ref 16). The axial velocities of these injected particles were set to 10 m/s with three different radial velocities of −1.25, −2.5, and −3.75 m/s, which correspond to three injection angles of −7°, −14°, and −20°. Table 2 itemizes the specifications of the particles used in the simulation of particle thermal history. In the present model, the temperature of the droplet was assumed to be constant and uniform during the melting and evaporating processes. In other words, when the temperature of the particle/droplet exceeds the melting point, it suggested that the particle had been completely melted. Initial conditions for the simulation of droplet deformation are also listed in Table 1. The surface tension of 0.43 J/m^2 of zirconia was used (Ref 17). The viscosity (η) of zirconia was calculated using Eq 1 (Ref 18) as a function of temperature, and the thermal contact resistance between the droplet and the substrate (R_s) was assumed to be 1×10^{-5} W/m^2 K (Ref 18). The contact angle between the droplet and the substrate (θ) was assumed to be 45°.

Table 2 Particle specifications for particle thermal history simulation

Index number	Initial size, μm	Axial velocity, m/s	Radial velocity, m/s	Sphericity
1	63	10	+1.25	1
2	63	10	+1.25	0.8
3	63	10	+1.25	0.9
4	63	10	+2.5	1
5	63	10	+2.5	0.8
6	63	10	+2.5	0.9
7	63	10	+3.75	1
8	63	10	+3.75	0.8
9	63	10	+3.75	0.9
10	71	10	+1.25	1
11	71	10	+1.25	0.8
12	71	10	+1.25	0.9
13	71	10	+2.5	1
14	71	10	+2.5	0.8
15	71	10	+2.5	0.9
16	71	10	+3.75	1
17	71	10	+3.75	0.8
18	71	10	+3.75	0.9
19	79	10	+1.25	1
20	79	10	+1.25	0.8
21	79	10	+1.25	0.9
22	79	10	+2.5	1
23	79	10	+2.5	0.8
24	79	10	+2.5	0.9
25	79	10	+3.75	1
26	79	10	+3.75	0.8
27	79	10	+3.75	0.9
28	88	10	+1.25	1
29	88	10	+1.25	0.8
30	88	10	+1.25	0.9
31	88	10	+2.5	1
32	88	10	+2.5	0.8
33	88	10	+2.5	0.9
34	88	10	+3.75	1
35	88	10	+3.75	0.8
36	88	10	+3.75	0.9

2.3 Results and Discussion

2.3.1 Flow Field without Powder Injection. Figure 2 shows the temperature and axial velocity contours of the hybrid plasma flames with RF input powers of 60 kW (Fig. 2a) and

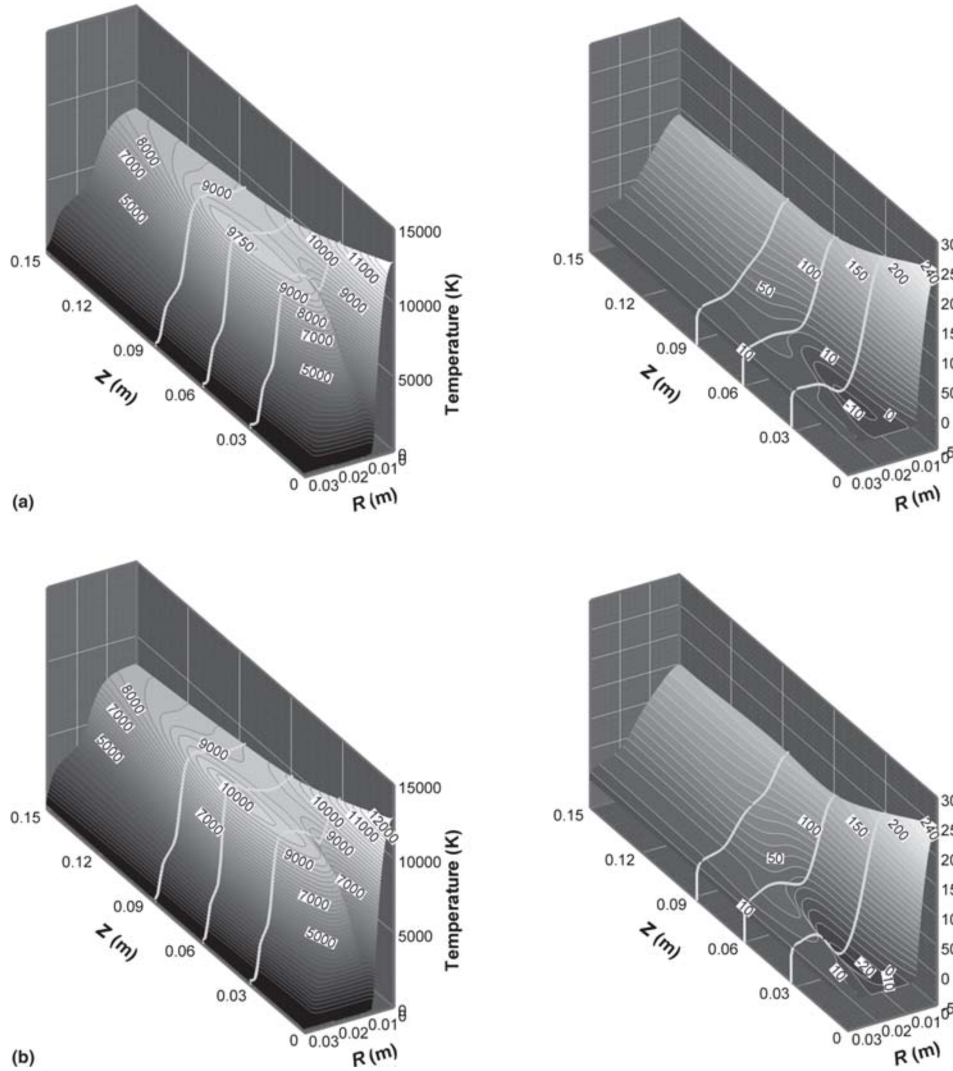

Fig. 2 Temperature and axial velocity contours of the hybrid plasmas without powder injection at RF input power of (a) 60 kW and (b) 100 kW. The three bold lines depict the slices at the three coil positions.

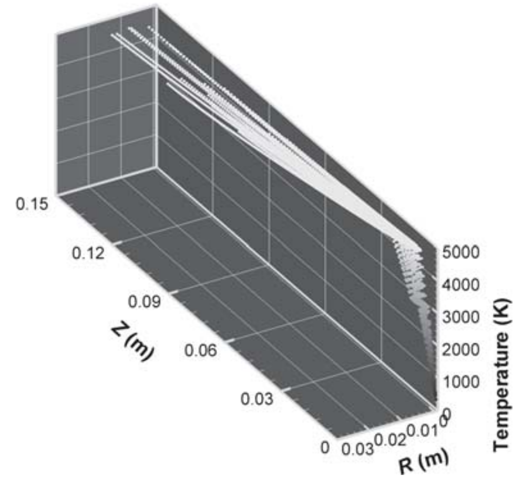

Fig. 3 Thermal histories of particles injected into a 60-kW hybrid plasma without considering the loading effect

100 kW (Fig. 2b). The large plasma volume, whose temperature is higher than 5000 K, and the center high-temperature and high-velocity zone caused by the DC plasma jet are characteristics of the hybrid plasmas (Ref 13). With higher input power, the plasma volume expands, which can be confirmed by the broadened higher temperature zone both at the coil region and at the torch exit, and thereby a slightly faster plasma flow is observed. The axial velocity of the plasma at the symmetry drops rapidly from 250 to 200 m/s when it reaches the coil region, where Z = 32 mm. At RF input power of 60 kW, this velocity continues to decrease slowly and monotonically to 138 m/s at the torch exit. At RF input power of 100 kW, this velocity reaches its first minimum value of 156 m/s; it then increases slightly and begins to decrease slowly and monotonically to 149 m/s at the torch exit. The negative value of the axial velocity between Z = 20 and 40 mm suggests the existence of a recirculation.

2.3.2 Particle Thermal History. Figure 3 shows the temperature histories of the particles injected into the 60-kW hybrid

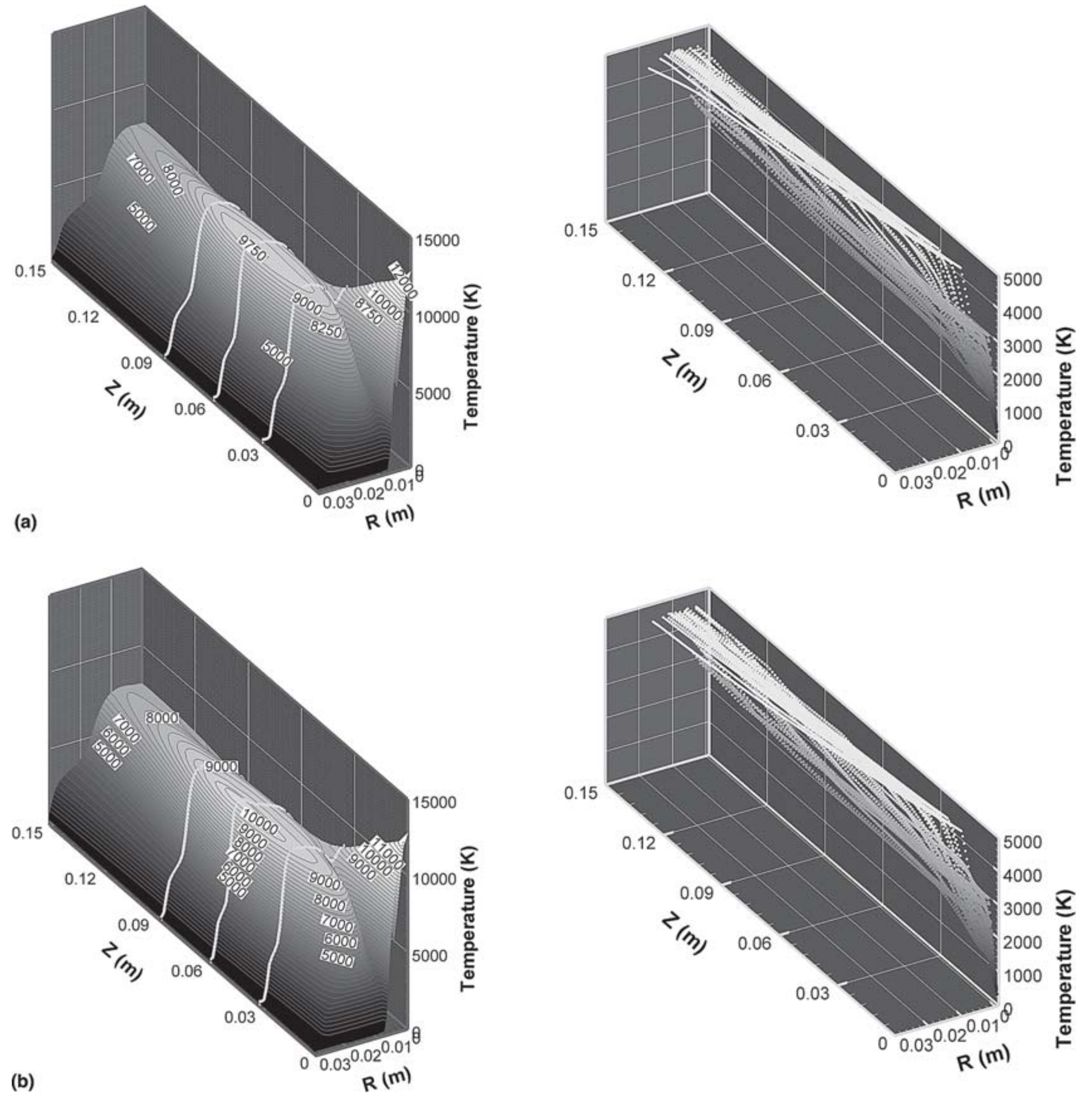

Fig. 4 Plasma temperature contours and particle thermal histories after 8 times coupling calculations with RF input power of (a) 60 kW and (b) 100 kW

plasma simulated in Fig. 2(a) without considering the loading effect. All of the particles are completely melted at the very beginning of the torch, where Z is only 15 mm, and the temperatures of all the droplets reach the boiling point of 4573 K in a very short time. Considering the drastic temperature difference between the particle and the environmental plasma, the injection of particles will certainly cause the plasma temperature to drop, particularly at the beginning of the torch where the particles are cold. In such cases, the loading effect should not be ignored. Figure 4 illustrates the temperatures of the hybrid plasma and the corresponding particles/droplets after eight iterations of coupling calculations at which convergence was attained. A significant temperature drop at the center zone of the plasma can be seen clearly. Compared with those in Fig. 3, the temperatures of the injected particles increase much more slowly when the loading effect is taken into account. Slices at both the coil center (Z = 60 mm) and the torch exit (Z = 150 mm) were extracted from the data to show the temperature (T_d) and axial velocity (u) distributions of the particles/droplets in these regions (Fig. 5). At RF input power of 60 kW, particles with index numbers of 20, 21, 29, 30, and 32 cannot be completely melted as their temperatures remain at or even below the melting point of 2973 K. Referring to Table 2, it is seen that such particles are mainly those with larger sizes and poorer sphericities that travel through the low-temperature zone of the plasma near the center. In the present model, the heat-transfer coefficient and the drag coefficient of the unmelted particle are correlated by the sphericity (Ref 16). Although better heating can be expected, the residence time of a particle with poorer sphericity is shorter due to the greater drag force, and thus leads to deficient melting. As can be seen in Fig. 5, the particles with initial poorer sphericities were accelerated more and thereby possessed higher velocities in the plasma. On the other hand, those particles that were completely melted were generally smaller in size with better sphericities and traveled through the high-temperature zone of the coil region. At 100 kW, all the particles injected were completely melted. Figure 6

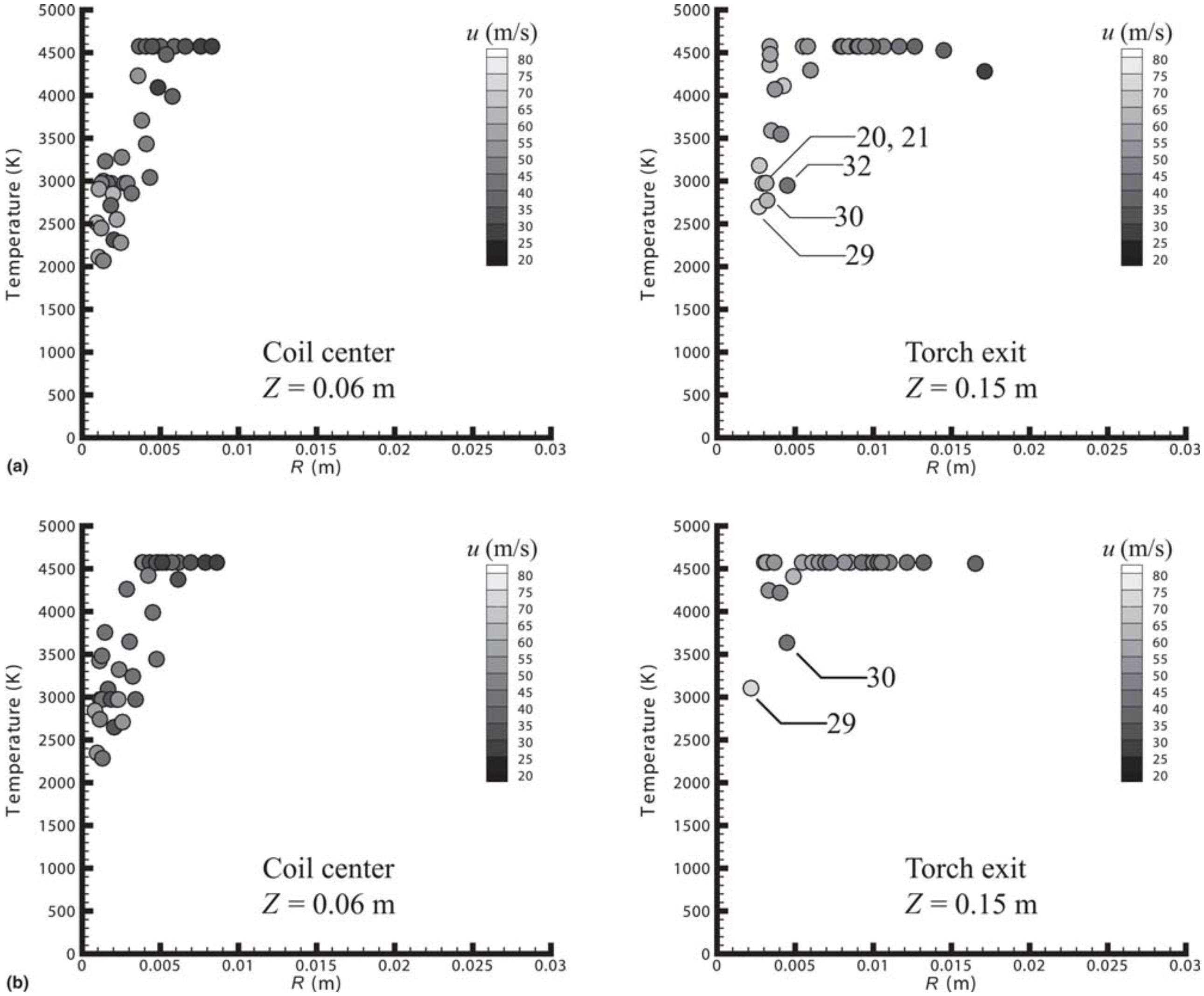

Fig. 5 Temperature and axial velocity distributions of the particles/droplets at the coil center ($Z = 0.06$ m) and at the torch exit ($Z = 0.15$ m) in the hybrid plasma with RF input power of (a) 60 kW and (b) 100 kW. The index numbers of the less-heated particles are marked.

shows the size distribution of the initial particles and the melted droplets at the exit of the torch. At a higher RF input power of 100 kW, more evaporation occurs, leading to smaller droplet size. Figure 7 summarizes the dependence of the temperature (T_d) and velocity (V_d) distributions of the droplets on their final sizes (d) at the torch exit. In Fig. 7(a), although all the particles injected into 100-kW hybrid plasma have been completely melted, there is a larger scattering of T_d at larger droplet sizes compared with all the small droplets below 50 μm having temperatures of 4573 K. However, this trend cannot be observed for the velocity distribution in Fig. 7(b). The initial smaller particles can be accelerated more rapidly than larger particles and therefore travel for a shorter time in the plasma, which leads to less evaporation and makes them similar in size at the torch exit with those larger particles that are slower and more intensively evaporated.

2.3.3 Single-Splat Deformation. In the present simulation, the droplet sizes (d), temperatures (T_d), and velocities (V_d) before impact were assumed to be in the same ranges as those at the torch exit obtained in the last section. Using these initial conditions, the flattening degrees (ξ) of the droplets were calculated, as shown in Fig. 8. Larger droplet size, higher temperature, and higher velocity result in the increased ξ. The data are shown as a 2-D plot in Fig. 9(a). In this study, the minimum flattening degree of a droplet was evaluated. When an extremely small and static droplet contacts a perfectly smooth substrate, the flattening of the droplet is considered to be dominated only by the wettability. In this case, the gravity of the extremely small droplet can be omitted compared with the force of surface tension, and the shape of the splat is considered to be a spherical cap. By identifying the volume of the initial droplet and the deformed spherical cap, Eq 2 was derived to describe such a minimum flattening degree at this extreme condition. In this simulation, because the contact angle (θ) was assumed to be 45°, the minimum flattening degree was then calculated to be 1.8, as marked by the circle in Fig. 9. The calculated ξ increases from 2.0 to 4.7 when the deformation occurs from a 30 μm, 3000 K, 10 m/s droplet to an 88 μm, 4573 K, 70 m/s droplet. The data was fitted using the empirical equation as $\xi = C\mathrm{Re}^{t}$ (Ref 19, 20), where *Re*

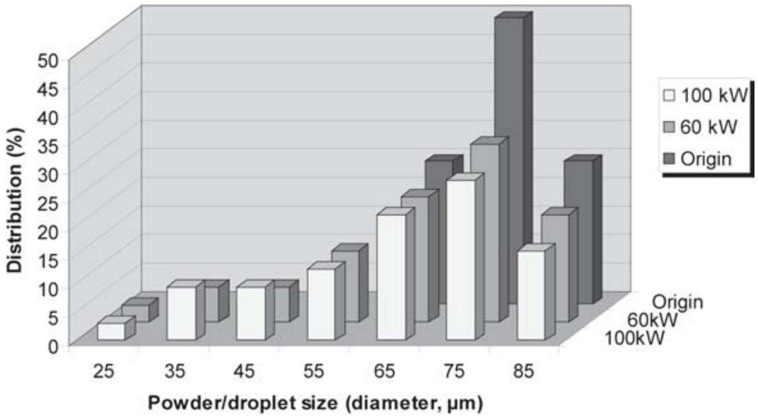

Fig. 6 Size distributions of the initial particles and the melted droplets at the torch exit

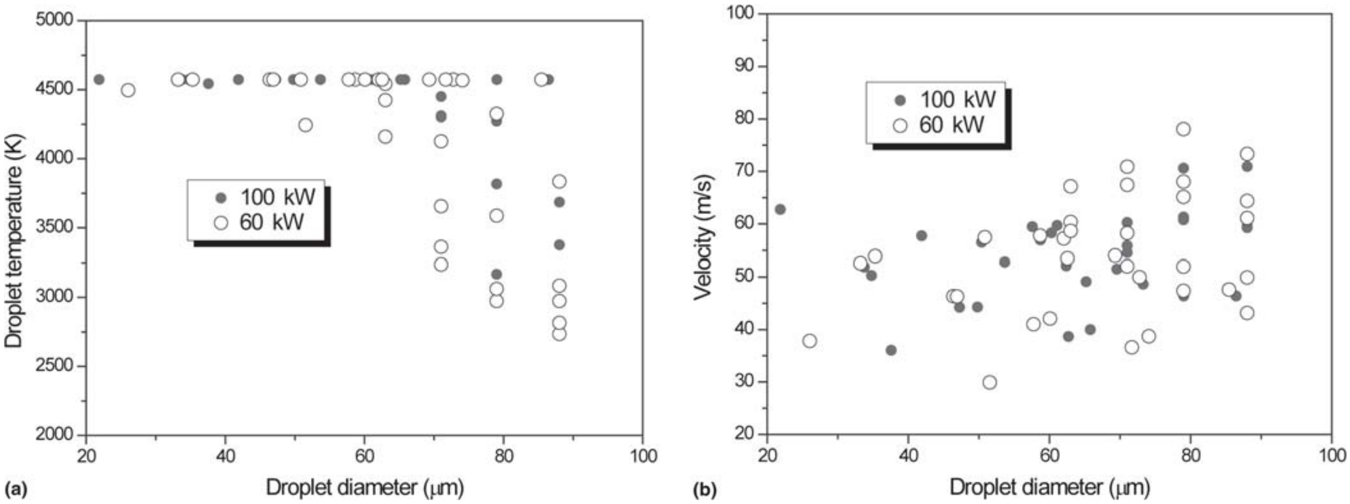

Fig. 7 (a) Temperature and (b) velocity distributions of the droplets with different sizes at the torch exit

is the Reynolds number and C and t are constants. Note that, in the empirical equation, the influence of surface tension was neglected and the liquid droplet was assumed to be completely flattened before solidification occurs, which is not the case in the present simulation. However, the fitted lines seem to be in reasonable agreement with the trends, with $C = 0.76 \pm 0.09$ and $t = 0.24 \pm 0.02$, as shown in Fig. 9(b). Even the proposed minimum flattening degree is not so aberrant.

2.4 Summary

Numerical simulations relating plasma generation, powder heating, and splat formation showed that:

- The hybrid plasma is characterized by the superposition of the temperature and velocity field of a DC arc jet and RF plasma. At a constant gas-flow condition, the temperature and velocity patterns of the hybrid plasma are affected by the input power.
- Zirconia particles as large as 63-88 μm can be fully melted with 100-kW RF power input, and the velocity of the melted droplets at the torch exit is in the range of 30-80 m/s. However, even in the hybrid plasma, a relatively wide distribution of the particle thermal history still exists, which can be narrowed by the elevated power input.
- Once the large powder has been fully melted, it can form better flattened splats than the small powder does, and the flattening degree is as large as 4.7.

These predictions were validated by the following experimental work.

3. Experimental Procedures

3.1 General

The objective of the present experiments is to investigate the actual behavior of the large YSZ powders in the high-power hybrid plasma spraying process. Using the same initial conditions as those in the numerical simulations, experiments of single-splat deformation and thick coating deposition were conducted.

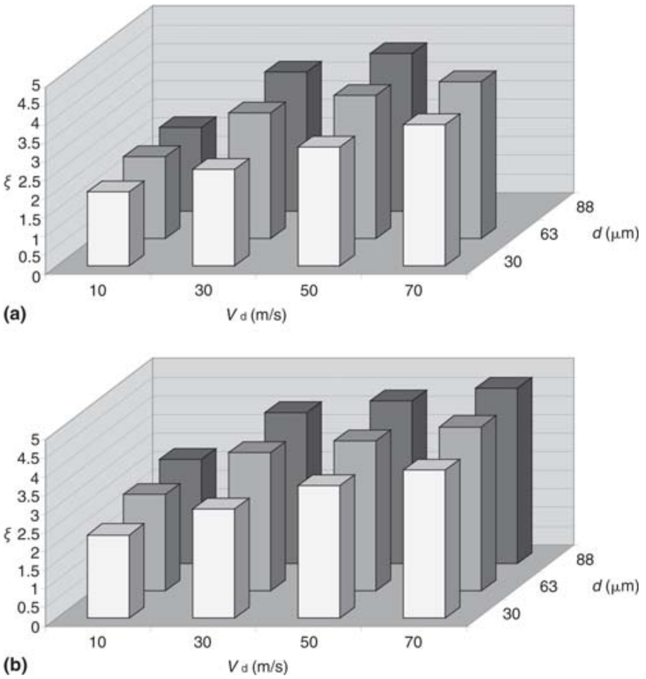

Fig. 8 Variation of flattening degree with droplet size and impinging velocity at temperatures of (a) 3000 K and (b) 4573 K

3.2 Experimental Details

The experimental parameters are listed in Table 1. In single-splat deformation experiments, the powder was injected into the torch after the prescribed temperature of the substrate was achieved. The feeding rate was lowered to 2 g/min and the deposition time was limited to less than 20 s to avoid overlapping of splats. As in the present experiments, because a rotary substrate holder was used (Ref 15), the percentage of the substrate covered in one turn of rotation (Λ) can be simplified in Eq 3, assuming that all the droplets disperse homogeneously in the hybrid plasma and adhere to the substrate after impact.

$$\eta = 0.0037 \exp\left(\frac{6100}{T}\right) \qquad \text{(Eq 1)}$$

$$\xi = \sin\theta \sqrt[3]{\frac{4}{\cos^3\theta - 3\cos\theta + 2}} \qquad \text{(Eq 2)}$$

$$\Lambda = \frac{6 f_p \xi^2}{\pi^2 D_p D_h d \rho} \qquad \text{(Eq 3)}$$

where F_p stands for the powder feeding rate, D_p the diameter of the plasma flame, D_h the diameter of the substrate holder, and n the substrate rotation speed. Λ is about 5% under the present experimental conditions, which means that 20 turns (24 s for the rotation speed of 50 rpm) are needed for the splats to cover the whole substrate surface. Polished stainless-steel substrates (R_a = 1.2 μm) of 5 × 5 × 4 mm in size were used for single-splat deformation experiments, and the thick YSZ coating was deposited on CoNiCrAlY-coated Inconel substrates. The backside temperature of the substrate was monitored using a thermocouple. Considering the heat flux and the thermal conductivity of the substrate, the estimated temperature gradient in the substrate was around 60 K/mm; thus the temperature difference between the surface and the backside of the substrate is about 250 K for the 4 mm thick substrates. In this research, therefore, the estimated substrate temperature (T_{es}) was used, which was 250 K higher than the measured backside temperature.

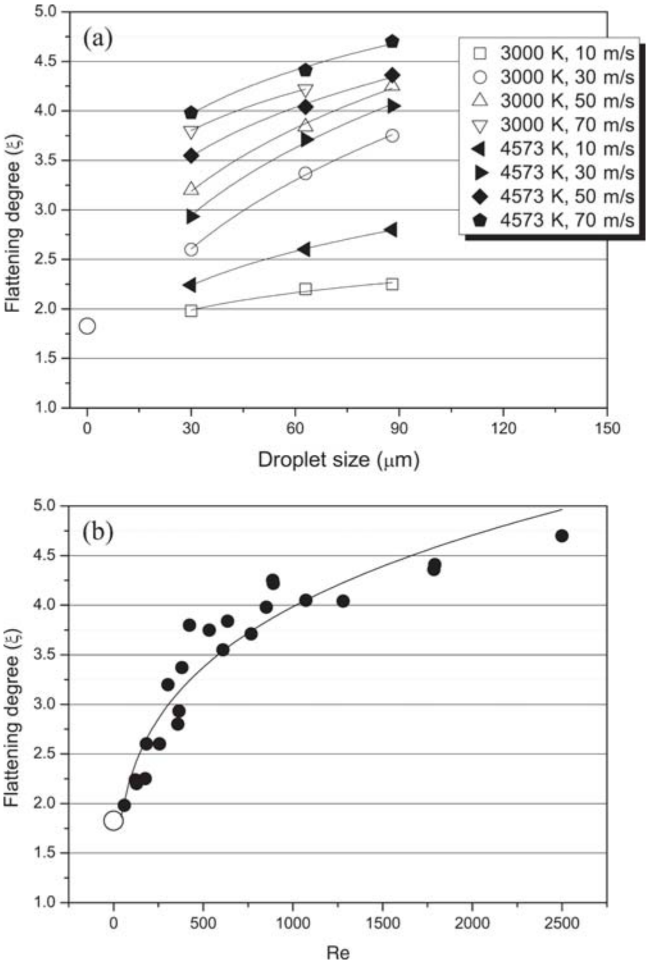

Fig. 9 Dependence of the simulated flattening degrees of the droplets on (a) the droplet size and (b) Reynolds number

A laser microscope (Keyence-VK8510, Japan) was used to observe the morphologies and to measure the height profiles of the splats. The crack density of a splat was evaluated by measuring the number of cracks along twenty 100 μm-long lines taken randomly. Cross-sectional microstructures of the splats and the deposited coating were observed using a focused ion beam scanning electron microscope (FIB-SEM, Micrion-2100, USA) and a field emission scanning electron microscope (FE-SEM, JEOL-F6340, Japan).

3.3 Results and Discussion

3.3.1 Single-Splat Deformation. Figure 10 shows splat morphologies at different estimated substrate temperatures (T_{es}). The droplet impinging onto a substrate with T_{es} = 823 K shows the most spherical morphology with a smooth surface. At a higher preheating substrate temperature (T_{es} = 1123 K), large

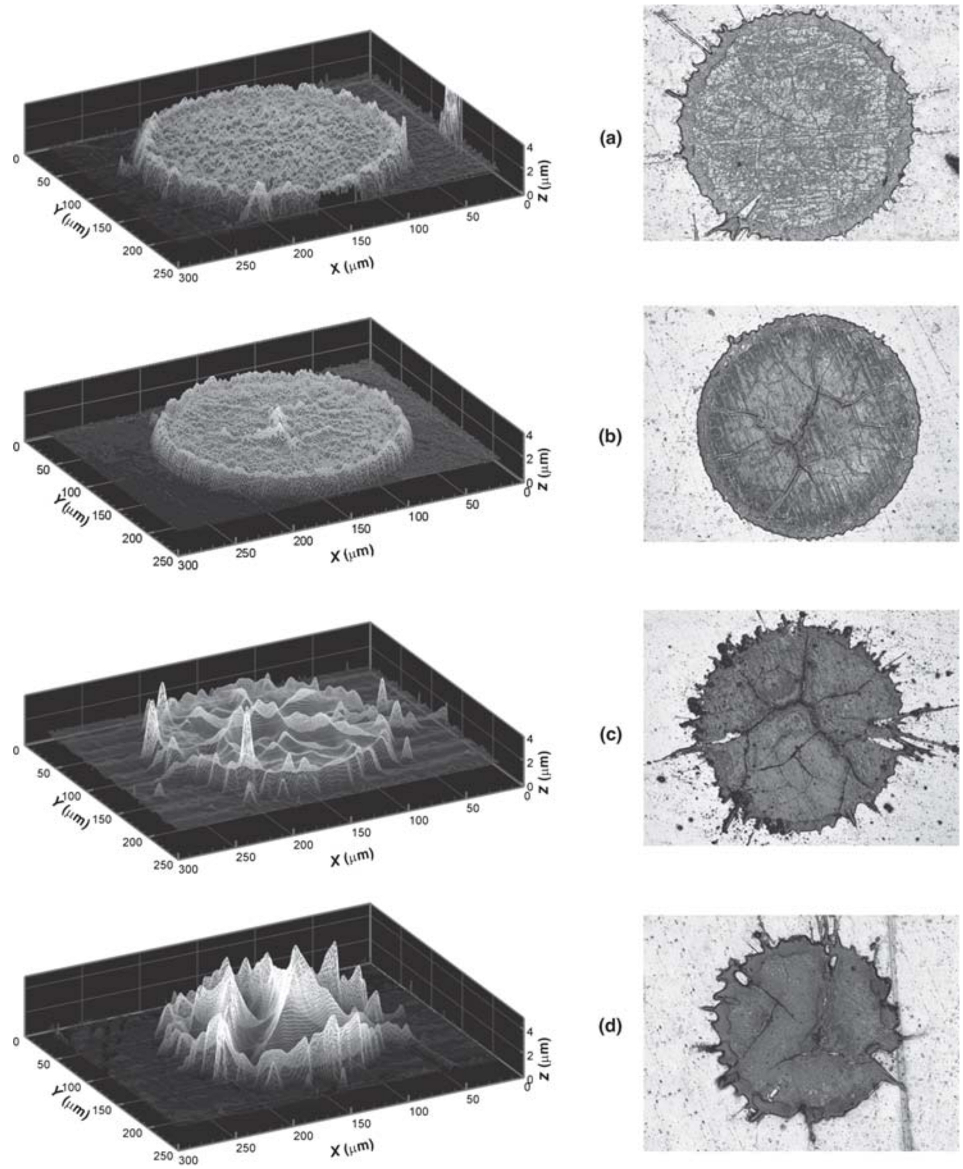

Fig. 10 Single-splat morphologies with different estimated substrate temperatures, T_{es}: (a) 723 K; (b) 823 K; (c) 923 K; (d) 1123 K

splats exhibit undulating surface morphology with cracks at the crests, as shown in Fig. 10(d). FIB observation was conducted near one of the crests (Fig. 11), revealing that a vertical crack was not associated with an interfacial crack between the splat and the substrate. A thin layer with smaller grains between the splat and the substrate was observed, and the originally smooth substrate rumples along with the shape of the splat. These facts are thought to be the result of substrate melting. Figure 11 also shows that some melted parts even filled into the vertical crack. Figure 12 depicts the variation of the crack density of the splats impinging on substrates with different T_{es}. When T_{es} = 823 K, the crack density of the splats increases from 3 to 9 until the splat diameter reaches around 250-300 μm, and then decreases slightly to 7 when the splat diameter becomes even larger. At T_{es} = 923 K, the crack density is much lower: it decreases monotonically from ~3.5 to 2.2 when the splat diameter changes from 150 to 350 μm. These crack density variations reflect the stress evolutions in the splat deformation process. Two factors that cause a tensile stress inside a splat: (a) the splat cools down from a much higher temperature than the substrate does, hence the splat contracts more than the substrate although its thermal expansion coefficient is smaller, and (b) due to the surface tension, the splat tries to rebound to its center after it spreads to its maximum diameter on the substrate. However, these processes are restricted by the adhesion at the splat/substrate interface. As mentioned above, adhesion is better when the droplet size is larger. Therefore, stronger tensile stress is expected in larger splats, which would lead to higher crack density. On the other hand, because the substrate temperature underneath the larger splats is higher, when substrate melting occurs, it somehow releases the tensile stress and thus causes a lower crack density. The convex trend of the crack density with splat size change

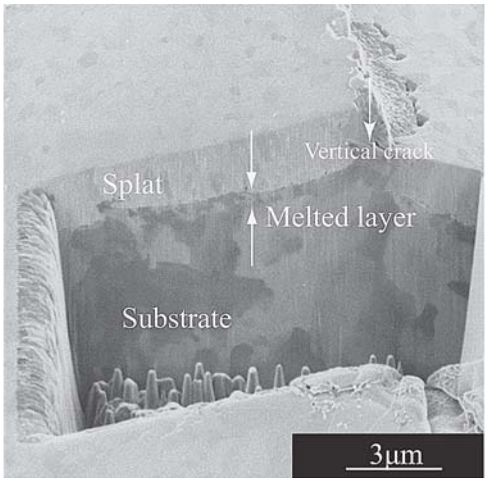

Fig. 11 Cross-sectional FIB micrograph of an undulant splat showing that substrate melting occurred with T_{es} = 1123 K

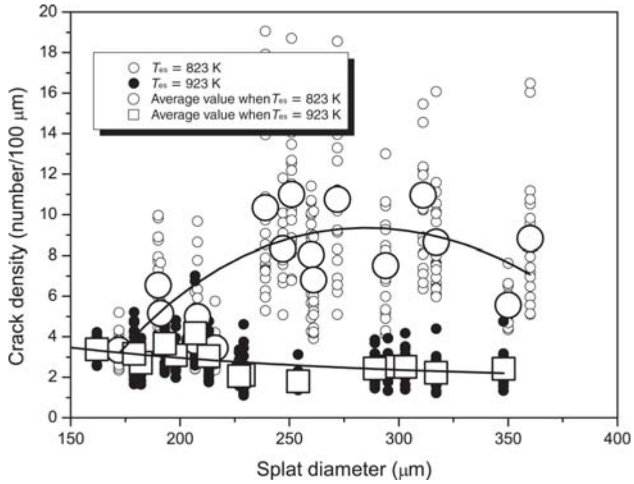

Fig. 12 Crack densities of the splats with T_{es} = 823 K and T_{es} = 923 K

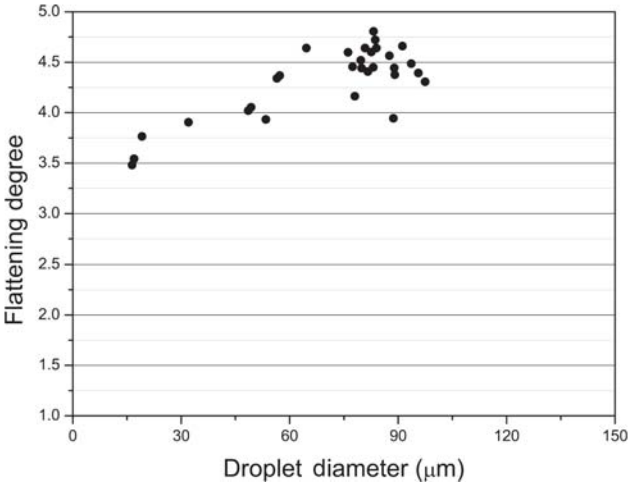

Fig. 13 Dependence of the flattening degree on the droplet diameter at T_{es} = 723 K

indicates that when T_{es} = 823 K, only the substrate under larger splats has been slightly melted. In contrast, when T_{es} = 923 K, substrate melting occurs even under small splats, which leads to lower crack density than that at T_{es} = 823 K, and also results in the inverse crack density dependence on splat sizes. As T_{es} = 823 K seems to be a critical temperature for the substrate melting, it is natural to consider that the melting condition depends on the positions at the interface between the splat and the substrate, which leads to localized crack density and shows a much wider distribution, especially for the mid-sized splats. In Fig. 12, a smaller average splat size can be seen as T_{es} increases, which also suggests that, at higher substrate temperatures, the splat contracts more than that at lower substrate temperatures. On the basis of these points, large splats deposited on a substrate with a temperature of 823 K are thought to be the best choice, due to their high adhesion strength, good surface morphology, proper crack density, and relative low tensile stress.

Figure 13 shows the measured flattening degrees at T_{es} = 723 K. The variations of flattening degrees at higher T_{es} are omitted because the undulating surface morphology causes large errors in splat volume measurements. When Fig. 13 is compared to Fig. 9(a), very good agreement between the experimental and simulation results is obtained. In Fig. 13, the flattening degrees of the smaller droplets are in the upper region of the simulation results in Fig. 9(a), indicating that the smaller droplets in the experimental work have higher initial temperatures and velocities. This conclusion can also be confirmed in Fig. 7, which shows higher temperatures of smaller droplets.

3.3.2 YSZ Coating Deposition. Figure 14(a) shows the cross section of a 300 μm thick YSZ coating sprayed by a 100-kW hybrid plasma using the large powders of size 63-88 μm. The preheating temperature was 823 K, and the temperature of substrate increases to 1100 K with time in the deposition process. The clean and crack-free interface indicates good adhesive strength between the YSZ top-coat and the CoNiCrAlY bond-coat (Fig. 14b). This suggests that the first layer of the coating is well deposited. Although the subsequent layers of the coating are deposited at a higher temperature (due to the low thermal conductivity of YSZ), they still show ultradense microstructure without clear boundaries between the splats because the droplets impinged onto the previous zirconia coating instead of the metal substrate, which may involve different deformation behaviors. Vertical cracks can also be observed in Fig. 14(b). Further research is needed to better understand the formation of the thick coating.

4. Conclusions

Numerical studies on the thermal history of large YSZ particles in high-power hybrid plasma and their deformation behaviors were performed to gain a better understanding of the basic phenomena involved in the hybrid plasma spraying and the particle-droplet-splat process. By using the high-power hybrid plasma, large YSZ powders can be completely melted and well flattened. They have stronger adhesion strength on the substrate and are promising for forming high-quality coatings. The results of single-splat deformation experiments and thick coating depo-

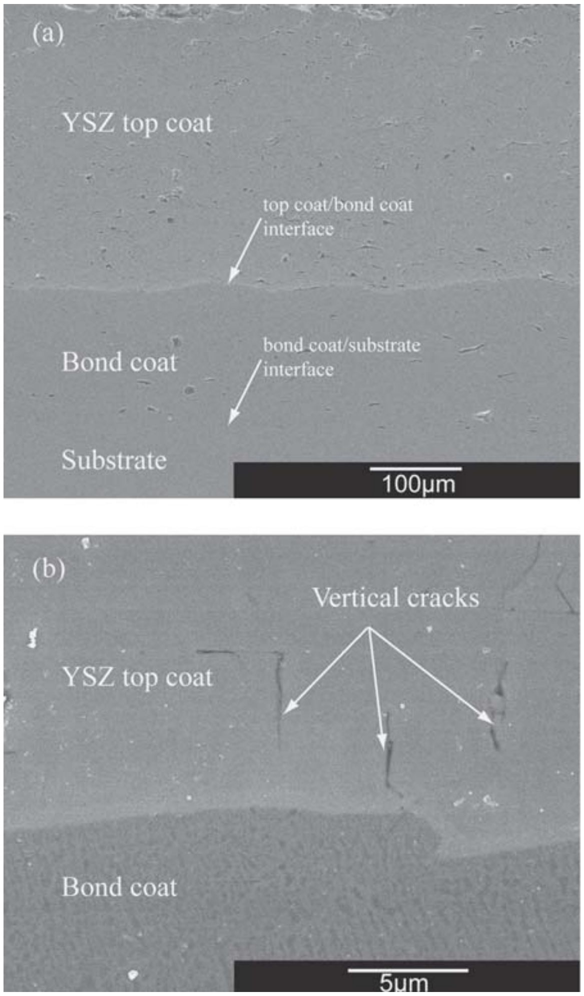

Fig. 14 Cross sections of large-particle plasma sprayed thick YSZ TBCs at (a) lower magnification and (b) higher magnification, showing dense microstructure and clean interfaces

sitions agree well with these predictions, which suggests that the viscosity of zirconia and the thermal contact resistance assumed in the simulations were reasonable under the present experimental conditions.

Acknowledgments

The present research is a part of the nano-coating project founded by NEDO. The authors express their deep gratitude to Dr. H. Paritz for helpful discussions on the simulation of particle thermal history and to Dr. Guotao Wu for his assistance in the experiment of single-splat deformation. One of the authors (H. Huang) gratefully acknowledges Marubun Corporation for supporting his research with the Marubun Research Promotion Foundation.

References

1. P. Fauchais, Understanding Plasma Spraying, *J. Phys. D: Appl. Phys.,* 2004, 37 (9), p R86-R108.
2. D. Clarke and C. Levi, Materials Design for the Next Generation Thermal Barrier Coatings, *Annu. Rev. Mater. Res.,* 2003, 33, p 383-417
3. N. Padture, M. Gell, and E. Jordan, Materials Science—Thermal Barrier Coatings for Gas-Turbine Engine Applications, *Science,* 2002, 296 (5566), p 280-284
4. L. Bianchi, A.C. Leger, M. Vardelle, A. Vardelle, and P. Fauchais, Splat Formation and Cooling of Plasma-Sprayed Zirconia, *Thin Solid Films,* 1997, 305 (1-2), p 35-47
5. M. Friis, C. Persson, and J. Wigren, Influence of Particle In-Flight Characteristics on the Microstructure of Atmospheric Plasma Sprayed Yttria Stabilized ZrO_2, *Surf. Coat. Technol.,* 2001, 141 (2-3), p 115-127
6. T.A. Taylor, Thermal Barrier Coating for Substrates and Process for Producing It, U.S. Patent 5,073,433, 1991
7. A. Kulkarni, A. Goland, H. Herman, A. Allen, J. Ilavsky, G. Long, C. Johnson, and J. Ruud, Microstructure-Property Correlations in Industrial Thermal Barrier Coatings, *J. Am. Ceram. Soc.,* 2004, 87 (7), p 1294-1300
8. Y.-C. Lau, H. Wang, and D.J. Mitchell, Method of Depositing a Compositionally-Graded Coating System, U.S. Patent 6,740,364, 2004
9. G. Farmer, Method of Protecting Gas Turbine Combustor Components against Water Erosion and Hot Corrosion, U.S. Patent 6,047,539, 2000
10. Y. Chae, T. Yoshida, and J. Mostaghimi, Deformation and Solidification Process of a Super-Cooled Droplet Impacting on the Substrate under Plasma Spraying Conditions, *Sci. Technol. Adv. Mater.,* 2000, 1, p 147-156
11. T. Yoshida, The Future of Thermal Plasma Processing for Coating, *Pure Appl. Chem.,* 1994, 66 (6), p 1223-1230
12. T. Yoshida, Some Issues for the Development of Spraying Technology, *Mater. Jpn.,* 2001, 40 (4), p 322-325
13. T. Yoshida, T. Tani, H. Nishimura, and K. Akashi, Characterization of a Hybrid Plasma and its Application to a Chemical Synthesis, *J. Appl. Phys.,* 1983, 54 (2), p 640-646
14. J. Mostaghimi and H. Parizi, A Model for the Hybrid Plasma Reactor, Company Report, Simulent, Inc., 203 College St., Unit 302, Toronto, Ontario M5T 1P9, Canada, 2003
15. H. Huang, K. Eguchi, and T. Yoshida, Novel Structured Yttria-Stabilized Zirconia Coatings Fabricated by Hybrid Thermal Plasma Spraying, *Sci. Technol. Adv. Mater.,* 2003, 4, p 617-622
16. Y.C. Lee, K.C. Hsu, and E. Pfender, Modeling of Particles Injected into a D.C. Plasma Jet, *Fifth International Symposium on Plasma Chemistry, 1981*, Edinburgh, U.K., 1981
17. J. Lihrmann and J. Haggerty, Surface Tensions of Alumina-Containing Liquids, *J. Am. Ceram. Soc.,* 1985, 68 (2), p 81-85
18. K. Shinoda, Y. Kojima, and T. Yoshida, In-Situ Measurement System for Deformation and Solidification Phenomena of Plasma-Sprayed Zirconia Droplets, *J. Therm. Spray. Technol.,* 2005, in press
19. J. Madejski, Solidification of Droplets on a Cold Surface, *Int. J. Heat Mass Transfer,* 1976, 19 (9), p 1009-1013
20. J. Madejski, Solidification of Liquid Sprayed Surface of Semispace, *Bull. Acad. Pol. Sci. Technol.,* 1976, 24 (1), p 67-70